Combinatorial material preparation

2002 J. Phys.: Condens. Matter 14 R49

(http://iopscience.iop.org/0953-8984/14/2/202)

INSTITUTE OF PHYSICS PUBLISHING JOURNAL OF PHYSICS: CONDENSED MATTER

J. Phys.: Condens. Matter **14** (2002) R49–R78 PII: S0953-8984(02)03634-2

TOPICAL REVIEW

Combinatorial material preparation

Young K Yoo[1] **and X-D Xiang**[2]

[1] Intematix Corporation, 351 Rheem Boulevard, Moraga, CA 94556, USA
[2] SRI International, Physical Science Division, 333 Ravenswood Avenue, Menlo Park, CA 94025, USA

Received 20 July 2001
Published 13 December 2001
Online at stacks.iop.org/JPhysCM/14/R49

Abstract

A high-throughput and systematic study of complex material systems is described. Initial efforts using thin-film discrete material chips are briefly reviewed from the perspective of materials discovery and optimization, and the limitations of the method are discussed. We then focus our discussion on the experimental techniques based on 'continuous phase diagrams' (CPDs) for epitaxial growth of thin films, and mapping their physical properties in two different material systems: perovskite manganese oxides and $Ni_{1-x}Fe_x$ metal alloys. For the former, we discuss the results of mapping optical, electrical, and magnetic properties of manganese oxides as functions of doping concentration, ionic radius, etc. We discuss the surprising evidence that suggests various electronic phase transitions, such as orbital orderings and smectic phase formation, in this highly correlated electronic system. For $Ni_{1-x}Fe_x$ metal alloy, we discuss a different application of the CPD in describing the structure–property relation of traditional materials science.

(Some figures in this article are in colour only in the electronic version)

Contents

1. Introduction 49
2. Discrete-composition material chips 50
   2.1. Early work: a proof of principle using discrete material chips 52
   2.2. Discovery of CMR in cobalt oxides using combinatorial material chips 55
3. Continuous phase diagrams 56
   3.1. CPDs of perovskite manganites 58
   Orbital ordering in doped Mott insulators. 67
   Anisotropic charge orders and stripes in doped Mott insulators. 71
   3.2. CPDs of structure–property relations of $Fe_{1-x}Ni_x$ metallic alloys 73
4. Conclusions 75
   Acknowledgments 76
   References 76

1. Introduction

Understanding complex systems is a major challenge in the 21st century science. Historically, the scope of materials research has been mostly limited to single-element or binary systems. The discovery of high-temperature superconductors in 1986 greatly accelerated our process of exploration into complex materials systems. With rapidly growing demands for better functional materials from high-technology industries, complex materials are receiving increasingly more attention in the materials research community. As a consequence, the basic research efforts in condensed matter physics are also driven toward more complex aspects of phenomena in condensed matter systems.

One such example is for highly correlated electronic systems. In these systems, the strength of the electron–electron interactions is comparable to the kinetic energy of the electrons. The effects of strong inter-electron interactions give rise to remarkably rich physics, producing phenomena such as the fractional quantum Hall effect, colossal magnetoresistivity, and high-temperature superconductivity. Modelling of these systems has proven difficult since the strong electron–electron interactions reduce the applicability of field theoretic methods (the quasi-particle approximation is no longer accurate). The experimental challenges are equally daunting. In the past, the discovery of materials exhibiting these phenomena was very often serendipitous. It took more than 70 years for scientists to discover high-temperature superconductivity after the initial discovery of superconductivity in 1911. While the original discovery involved simple one-element metal systems, the high-temperature superconductivity was initially found in multi-component (more than four elements) oxide systems. Obviously the discovery process gets even more difficult and time-consuming when the materials include more elements. In addition, conventional studies are usually performed on individual samples of discrete compositions, often missing the subtle details and important correlations between different compositions.

The development of more effective and systematic methods to explore complex systems is therefore critical to changing this situation. This effort is important for theoretical understanding of the complex system. If we take the case of high-temperature superconductivity, nothing in the history of science provoked such an intense and concentrated global research effort as the attempts to solve this problem. The euphoria just after the discovery is still fresh in our memory, but one wonders, after 15 years of intense global effort, whether we are going to reach a point of understanding of the underlying microscopic mechanism any time soon. Lack of reliable, thorough, and systematic experimental data to guide the theoretical efforts should be partially blamed for this situation.

In view of these observations, we have in the past seven years carried out a systematic research effort to develop methods and techniques that promise to dramatically change the situation. In our initial efforts, the discovery aspect of the exploration was emphasized. The experimental approach (mainly the discrete-material-chip technique) was designed to explore a multi-component phase space as broad as possible. These high-throughput research efforts were extensively discussed in previous review papers [1, 2]. In the next section, we briefly describe these studies for two selected systems of interest: superconductors and magnetoresistive materials. It soon became apparent that this approach has very limited use in studying complex physics phenomena. We then adopted a more thorough and systematic approach, i.e., the continuous phase mapping of physical properties using an epitaxial thin-film CPD growth technique and various high-throughput and high-resolution screening tools. We discuss our efforts in this direction in section 3.

2. Discrete-composition material chips

An analysis of the critical temperature of the known superconductors shows a clear increase in T_c with increasing chemical complexity [3]. One explanation for this observation is that more complex structures offer more tunability in crystal chemistry for optimizing certain properties. However, among the 24 000 known inorganic phases, as estimated by Phillips in 1989, only 8000 are ternary compounds, compared with 16 000 binary compounds [4]. When compared with the roughly 100 000 ternary compounds that one might reasonably make, given only one stoichiometry of each, it becomes clear that large numbers of compositions have yet to be examined for superconductivity. Higher-order materials, such as the quaternary compound $YBa_2Cu_3O_{7-\delta}$, increase the number of possibilities even further. Although these higher-order materials have the highest T_cs, the least work has been done on such systems. In fact, the quaternary compound $YBa_2Cu_3O_{7-\delta}$ (the first superconductor with a T_c exceeding liquid-N_2 temperature) is not only the first quaternary superconductor, but also the first quaternary metal oxide ever found [4].

Because of the overwhelming numbers of compositions that must be searched through to find new classes of superconductors, most of the previous efforts were limited to compositions and structures related to known compounds. Elements are replaced one at a time by a time-consuming trial-and-error process. Most of the attention until 1986 focused on intermetallic compounds such as Nb_3Ge. Few people considered oxides as reasonable candidates until the serendipitous discovery of the $La_{2-x}Sr_xCuO_4$ superconductor. Shortly thereafter it was found that introduction of yttrium, i.e., producing $YBa_2Cu_3O_{7-\delta}$, increases the T_c to 93 K [5]. However, this superconductor, in contrast to expectation, had a new structure as well. Although the Bi, Tl, and Hg copper oxide superconductors have relatively similar structures, it took five years of intensive effort to find them. Indeed, relatively little effort has been spent searching through, for example, higher-order bismuth oxides for superconductivity, in spite of the report of a $Ba_{1-x}K_xBiO_{3-\delta}$ superconductor with a T_c above 30 K [6].

The search is further complicated by the relatively poor state of synthetic methods (in

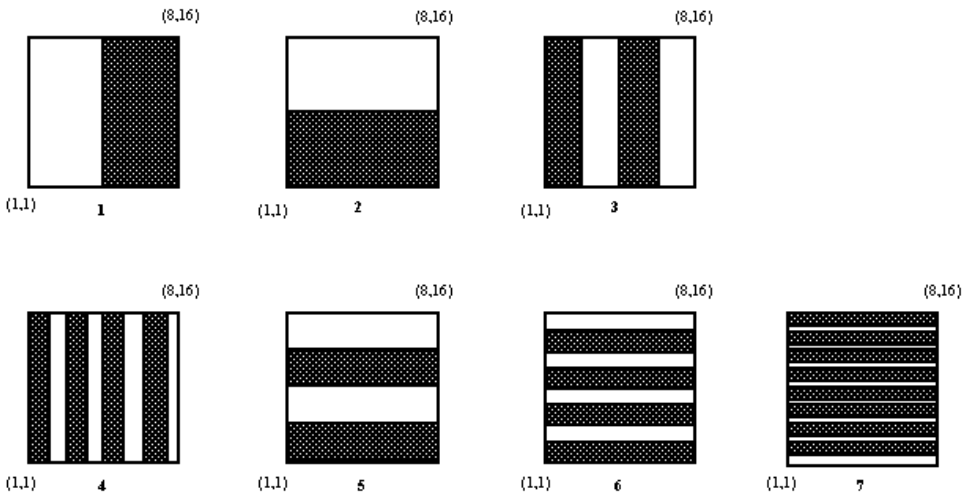

Figure 1. Binary masks used for library synthesis. Numbers in the lower left hand and upper right hand corners indicate the positions of each member in the library. M0 corresponds to no secondary mask (reproduced from [7]).

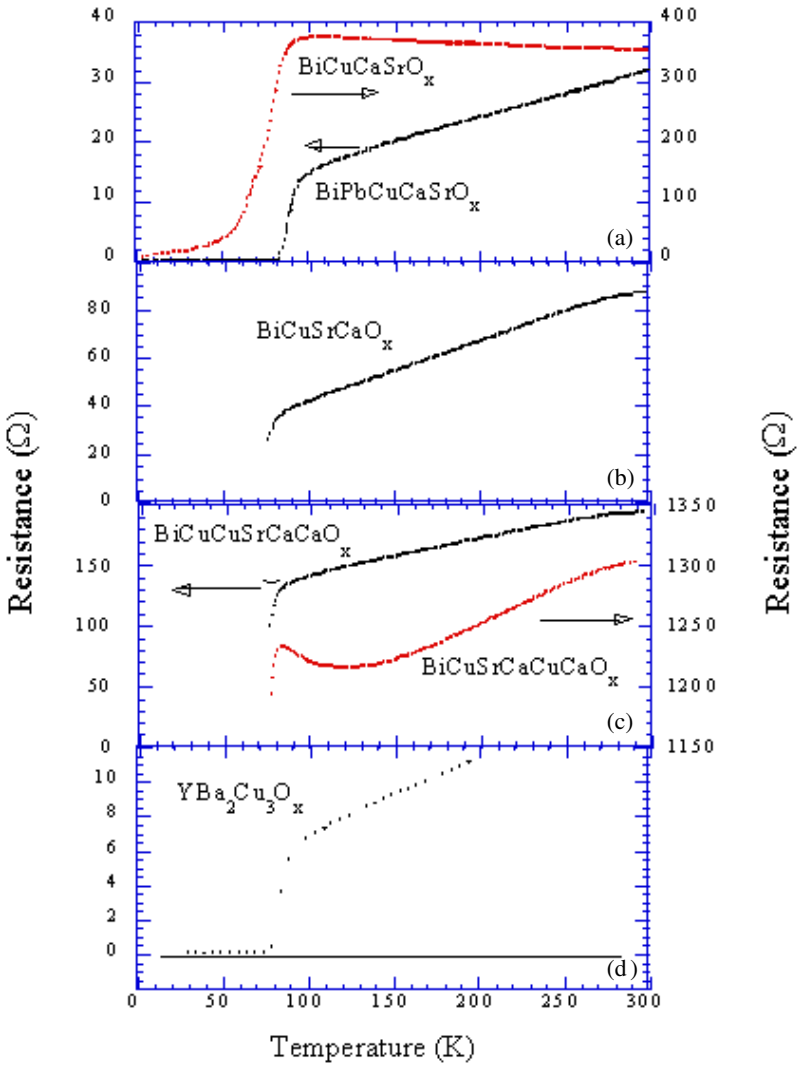

Figure 2. Resistivity versus temperature plots: (a) BiPbCuCaSrO; BiCuCaSrO; (b) BiCuSrCaO; (c) BiCuSrCaCuCaO; BiCuCuSrCaCaOn; (d) $YBa_2Cu_3O_x$ (reproduced from [7]).

comparison to the situation in organic chemistry, where virtually any structure can be rationally synthesized) and the lack of a firm theoretical basis for correlating superconductivity with structure, or even for the possibility of forming certain structures. Therefore, a combinatorial approach involving the synthesis and screening of a large phase space of solid-state materials could have a dramatic impact on the search for new classes of superconductors with enhanced properties. Of course, empirical observations, structural knowledge, theory, and intuition should all be used to guide the design of the combinatorial material chips.

Figure 3. The 128-member binary library prior to sintering. The dimension of each sample is 1×2 mm^2. The colour of each is the natural colour of light reflected from a white-light source (reproduced from [7]).

2.1. Early work: a proof of principle using discrete material chips

We conducted our early study in 1994 to demonstrate the feasibility of using a combinatorial approach to search for copper oxide superconductor [7]. In this study, we tried to answer the following question: if the technique was available ten years ago, could we have used it to discover YBCO and BSCCO superconductors after the initial discovery of $La_{1-x}Sr_xCuO_4$?

Two factors were considered initially in developing our early techniques. First, methods were devised to rapidly generate a large number of spatially addressable arrays of solid-state materials on a single substrate in a form assessable by screening techniques, and thereby to speed up both the synthesis and the characterization process. Secondly, the methods should be compatible with non-conventional solid-state synthetic methods that will allow us to produce not only thermodynamically stable but also metastable phases. This consideration has led us to choose a thin-film deposition/synthesis method to generate a large collection of different compositions.

A 128-member discrete material chip was generated by depositing precursors of $BaCO_3$, Y_2O_3, Bi_2O_3, CaO, $SrCO_3$, and CuO through series binary masks using a RF magnetron sputtering gun. The ratio of each precursor was simply kept at 1:1 to avoid much after-the-fact knowledge being used in the design. Film deposition thickness was monitored with a crystal microbalance and calibrated independently with a profilometer. The uniformity of the deposited films varies by approximately 5% over a two-inch-diameter area. MgO single crystals with a [100] polished surface were used as substrates and CuO, Bi_2O_3, CaO, PbO, and $SrCO_3$ were used as sputtering targets. The library was generated using a binary masking strategy (figure 1). Precursors were sputtered through the appropriate binary mask in a stepwise fashion. In a binary synthesis, 2^n compounds are formed for a given number of masking steps (n). The array contains all combinations that can be formed by deleting one or more steps from the entire deposition/masking sequence.

The fact that libraries are generated by sequentially depositing precursors as thin films, this being followed by solid-state reaction, distinguishes this approach from conventional

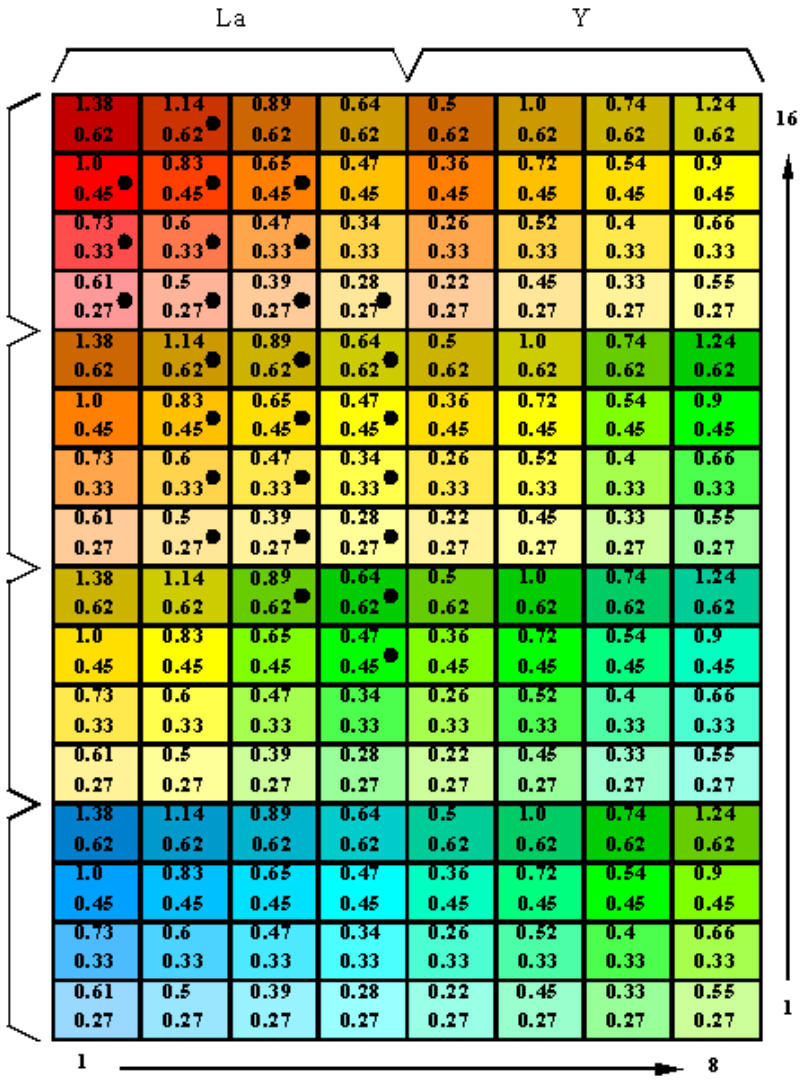

Figure 4. A map of compositions and stoichiometries for ($Ln_xM_yCoO_{3-\delta}$, where Ln = La and Y and M = Ba, Sr, Ca, and Pb) of thin-film samples in libraries L1 and L2. Samples are labelled by index (row number, column number) in the text and figure caption. The first number in each box indicates x and the second y. Solid circles indicate the samples that show significant MR effects (>5%) (reproduced from [8]).

bulk synthesis and thin-film fabrication methods. Special processing is needed for proper interdiffusion between precursor layers and subsequent crystalline phase formation. For example, in order to synthesize the $YBa_2Cu_3O_{7-x}$ superconductor from a film generated by sequentially depositing BaF_2, Y_2O_3, and CuO in a 1:2:3 molar ratio (∼400 Å of CuO), it was necessary to anneal samples at low temperature (200–400 °C) for an extensive period prior to high-temperature (840 °C) sintering. The diffusion process at low temperatures facilitates the formation of a homogeneous amorphous intermediate without nucleation of stable lower-order phases.

Initially a material chip of sixteen different members was generated. The resistance of each site was measured using an in-line four-probe configuration. Two films were found to be superconducting and the resistance of each was measured as a function of temperature down to 4.2 K in a liquid-helium cryostat. The critical temperatures (T_c) of the BiCuCaSrO and BiPbCuCaSrO films were 80 and 90 K, respectively, as shown in figure 2(a). The BiPbCuCaSrO sample has a metallic resistivity from room temperature to about 100 K, whereas the resistivity of the BiCuCaSrO film increases slowly with decreasing temperature down to the critical temperature. The T_cs as well as the x-ray diffraction patterns of these samples are consistent with those reported in the literature for $Bi_2Sr_2Ca_1Cu_2O_8$.

A 128-member chip was then generated for further examining the effects of stoichiometry and deposition sequence on the properties of the BiSrCaCuO films (figure 3). In general, films with low resistivities showed metallic behaviour with onset T_cs of 80–90 K. Films with excess Ca and Cu (Bi:Sr:Ca:Cu ratios of 2:2:4:4 and 2:2:4:5) showed a 110 K phase, consistent with the formation of $Bi_2Sr_2Ca_2Cu_3O_{10}$. A number of films with identical stoichiometries but different deposition sequences displayed distinct resistivity versus temperature profiles (e.g., BiCuSrCaCuCaO and BiCuCuSrCaCaO in figures 2(b) and 2(c)), suggesting that different phases may be accessible by controlling the sequence in which the layers diffuse.

Although the proof of concept of our technique was first demonstrated in copper oxide superconductors, using the approach of realistically searching for new superconductors still represents the most challenging task. Not only do we have few guidelines to follow as to where to search, but also we have to implement sensitive screening techniques at cryogenic temperatures. Implementing scanning evanescent microwave probes (EMPs), magneto-optical imaging systems, and scanning SQUIDS at low temperatures to perform non-contact electrical and Meissner effect measurements is under consideration.

2.2. Discovery of CMR in cobalt oxides using combinatorial material chips

Soon after the first proof of principle in superconductors, we used materials chips to identify a class of cobalt oxide magnetoresistive materials of the form $(La_{1-x}Sr_x)CoO_3$ [8]. Prior to this study, large magnetoresistances were found only in Mn-based perovskites, $(La, R)_{1-x}A_xMnO_{3-d}$, where R = rare earth, and A = Ca, Sr, Ba. The question arises of whether these effects are unique to Mn-based perovskite oxides or can be found as an intrinsic property of other materials. An analysis of the effects of spin configuration and electronic structure on the magnetoresistive properties of the other transition-metal-based compounds should help to elucidate the underlying mechanism of the CMR effect. Moreover, the discovery of diverse classes of CMR materials may help significantly in efforts to optimize these materials for eventual device applications.

Using materials chips, we searched through the simple perovskite ABO_3 and related A_2BO_4 or $A_{n+1}B_nO_{3n+1}$ higher-order structures, where A = $(La, Y, \text{rare earth})^{3+}$ with partially substitution of $(Ca, Sr, Ba, Pb, Cd)^{2+}$ and B = (Mn, V, Co, Ni, Cr, Fe). A 128-member material chip was generated by combining sequential RF sputtering deposition of thin films with a series of physical masking steps designed to produce films containing Y, La, Ba, Sr, Ca, and Co (1 mm by 2 mm in size) with varying compositions and stoichiometries. A map, which indicates the composition and stoichiometry of each sample, is illustrated in figure 4. The resistivity of each sample as a function of magnetic field, perpendicular to the probing current, and temperature was measured using the four-probe contact method with a computer-controlled multi-channel switching system.

A number of films in the library showed a significant MR effect (>5%), and these are indicated in figure 4 by solid circles. Three compounds that exhibit a large GMR effect have

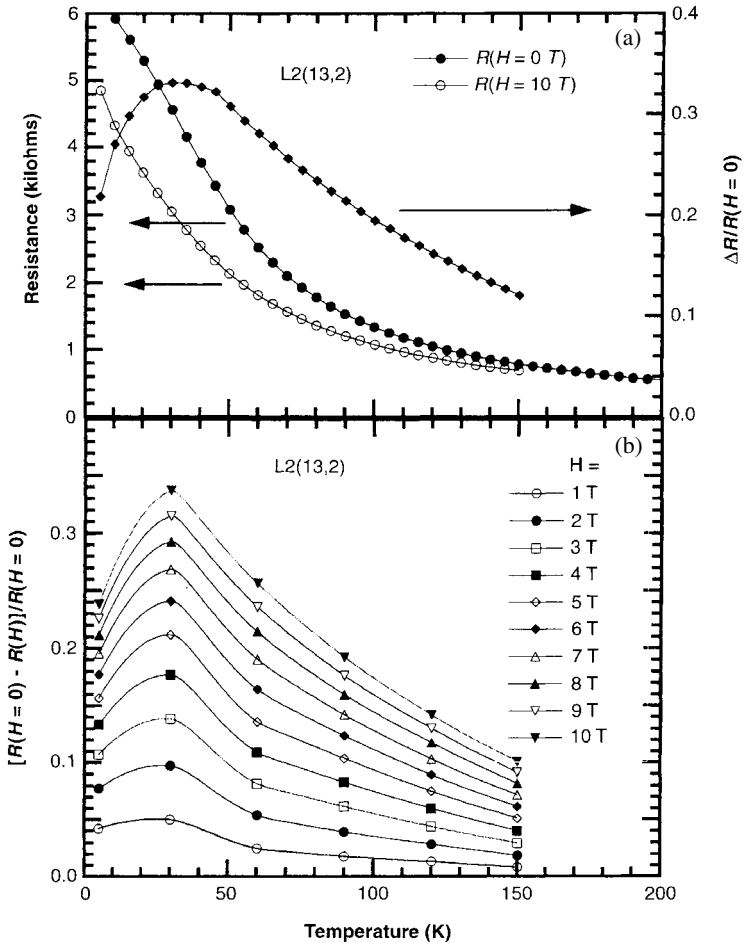

Figure 5. (a) Resistance of sample L2 (13, 2) under 0 T and 10 T and the MR ratio ($H = 10$ T) as a function of temperature; (b) MR ratios of the same sample for different magnetic fields as a function of temperature. The solid curves are guides to the eye (reproduced from [8]).

been identified: $La_xM_yCoO_\delta$ where M = Ca, Sr, Ba. The temperature dependence of the resistance and normalized MR of a representative sample L2 (13, 2) under different fields are shown in figure 5. In contrast to the behaviour of Mn oxide MR materials [9, 10], we found that the MR effect increases as the size of the alkaline-earth ion increases.

The MR effects of the samples in library L1 are larger than those for L2, presumably due to differences in oxidation resulting from slightly different thermal treatments. The normalized magnetoresistances of representative samples as a function of magnetic field at fixed temperature (60 K) are shown in figure 6. The largest MR ratio measured in this library was 72%, obtained for sample L1 (15, 2) at $T = 7$ K and $H = 10$ T. This value is comparable to those measured for films generated in a similar fashion in a Mn-based material chip. As with the manganese-containing materials, optimization of composition, stoichiometry, substrate, and synthetic conditions may lead to increases in the MR ratio. The corresponding Y–(Ba, Sr, Ca)–Co compounds show much smaller (<5%) MR effects.

This study has resulted in the discovery of a new family of Co-containing magnetoresistive

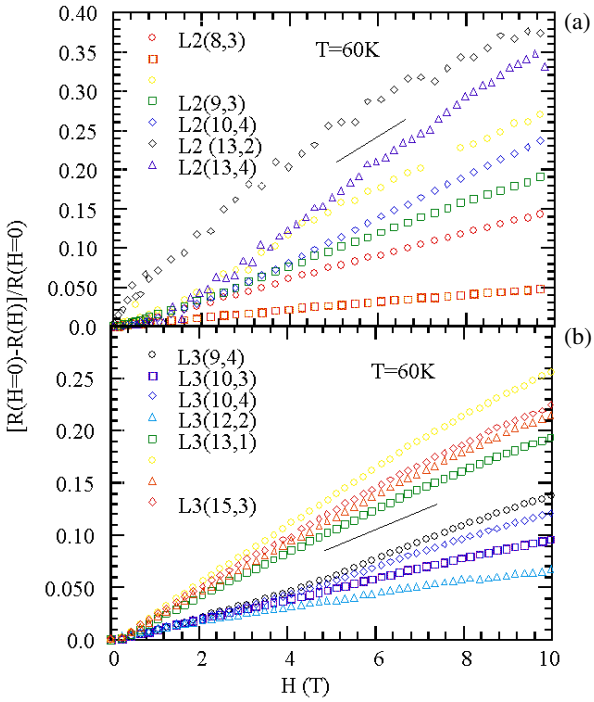

Figure 6. MR ratios of representative samples in L1 (a) and L2 (b) as a function of magnetic field (reproduced from [8]).

materials. Magnetoresistance was found to increase as the size of the alkaline ion increased, in contrast to the case for Mn-containing compounds, in which the magnetoresistive effect increases as the size of the alkaline-earth ion decreases. An analysis of the effects of spin configuration and electronic structure on the magnetoresistive properties of the Co- and Mn-based compounds should help to elucidate the underlying mechanism of the magnetoresistance effect.

3. Continuous phase diagrams

Mapping out phase diagrams has been the core subject in materials science and condensed matter physics. In materials science, the term 'phase diagram' most often refers to the structural phase diagram, i.e. formation of different crystal structures as functions of composition and temperature. In general and more importantly, if other physical properties are also mapped out together with the structural information, the phase diagrams should show the structural–property relationship, the central issue of materials science. However, in condensed matter physics, 'phase diagram' often refers to the mapping of fundamental physical properties as functions of parameters such as doping concentration and temperature. In these studies, physical phase transitions rather than structural phase transitions are emphasized.

Traditionally, phase mapping of structural and physical properties as a function of material composition was accomplished by the synthesis and analysis of samples with discrete compositions prepared and characterized one at a time. This process consumes extensive time and human resources. It also has very limited ability to provide detailed mapping due to intrinsic difficulties in producing identical growth conditions for all crystals and detecting

subtle differences in their physical properties. This lack of systematic and comparative studies may lead to many opportunities for important discoveries being missed.

Long before the recent activity in combinatorial materials science, there were some efforts among materials scientists and condensed matter physicists to partially address this problem. For example, diffusion couples and triples have been used to map the structural phase diagrams of binary and ternary systems [11]. This approach relies on the existence of a small diffused region (of the order of tens of microns) at the interface of multi-component systems after heat treatment. In this approach, the phase points being mapped out in a phase diagram are not evenly distributed in the cross section of the interface region. The key to the success of this approach is the capability of analytical tools to determine accurately the local composition and crystal structure with high spatial resolution (ideally much less than 1 μm). Electron-microscope-based techniques are often used for this application [12]. However, tools with similar resolution are not always available to characterize many other physical properties. As a consequence, the approach remains difficult to apply in mapping out physical properties.

The 'composition-spread' technique represents a different approach, which generates a map of varied composition in a large two-dimensional space. The earlier efforts to use this approach can be traced back to the work of Kennedy *et al* [13]. Due to a number of technical difficulties, the method has only been used to grow amorphous or polycrystalline samples. Another difficulty in this early effort was the lack of advanced screening tools. Recently, van Dover and his colleagues at Bell [14] Laboratory have improved the technique and applied it to solving important industrial materials problems. Usually, 'composition-spread' techniques rely on the geometric arrangement of target and substrate to generate composition gradients. As a result, the gradients are not linear, and vary with different precursors and deposition conditions. Time-consuming chemical analysis and coordinate transformation are usually required to generate a map (or phase diagram) conforming to standard binary or ternary representation. In addition, this method has been demonstrated to produce mainly amorphous alloy materials, which limited the ability to map out structural and physical phase diagrams.

Yoo [16–18] *et al* adopted a technique that generates a continuous phase diagram (CPD) in an epitaxial thin-film format. The technique first generates a linear gradient profile of a single element or a composite by moving precision masks for each individual precursor. By rotating the substrate after each deposition, binary or ternary phase diagram profiles can be generated. Subsequent low-temperature diffusion and high-temperature phase formation give rise to CPDs in a format of high quality, most often that of epitaxial crystalline film. This approach can produce a well-defined (usually in a linear fashion for direct phase diagram mapping) local composition in an area large enough for physical property characterization. On the other hand, the CPD is small enough to match available substrates of any experimenter's choice, often critical for growing high-quality crystalline films. These features are essential for reliable phase diagram mapping, which makes the CPD approach a significant improvement over the discrete-material-chip technique and other previous approaches. It can reveal, in a systematic way, the scientific phenomena of a given system often missed by the conventional approach.

3.1. CPDs of perovskite manganites

Manganese oxides belong to a class of highly correlated electronic systems where long-range Coulomb interaction between electrons gives rise to many-body correlation with a strong interplay between electronic and magnetic order. A central feature of this system is that it is a doped Mott insulator, obtained by chemically adding charge carriers to a highly correlated antiferromagnetic insulator (AFI). The behaviour of manganese oxides is strongly dependent on the charge filling (doping) and lattice parameter, which control the overlap of the electron

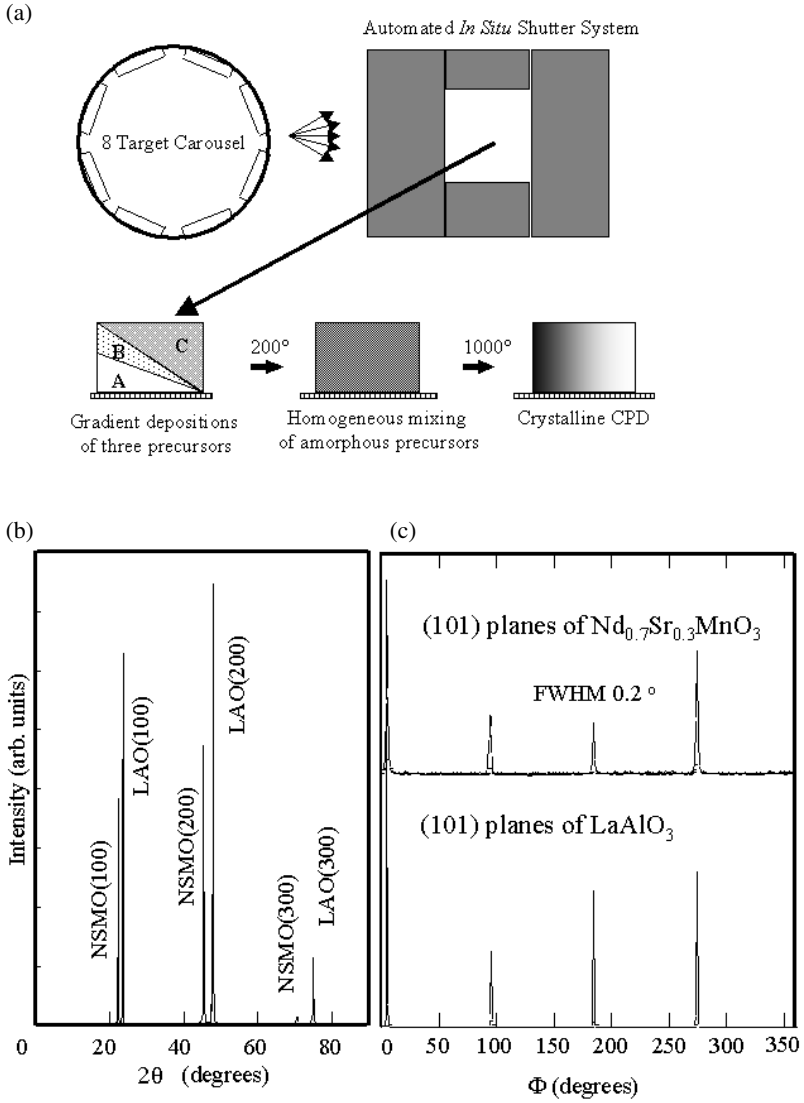

Figure 7. (a) High-precision *in situ* shutters in a PLD system. An eight-target carousel allows uninterrupted depositions without breaking the vacuum. Vertical shutters are used to define the width of each phase strip on a substrate while precise gradient profiles of three precursors are deposited with horizontal shutters moving across the phase strip at constant speed. (b) The $\theta/2\theta$ XRD pattern and (c) the ϕ-scan of the (101) plane of a $Nd_{0.7}Sr_{0.3}MnO_3$ (NSMO) thin film made from the three precursors Nd_2O_3, Mn_3O_4, and $SrMnO_3$ on (001) $LaAlO_3$.

wave functions.

The stability of the perovskite manganites against chemical substitutions provides an opportunity to study the effect of varying the parameter of a highly correlated electronic/magnetic system. In this study we control the charge filling n of a Mott insulator by continuous charge doping over the entire range, and the hopping integral t through the substrate-induced anisotropic strain effect in epitaxial films and the average ionic radius of the A site.

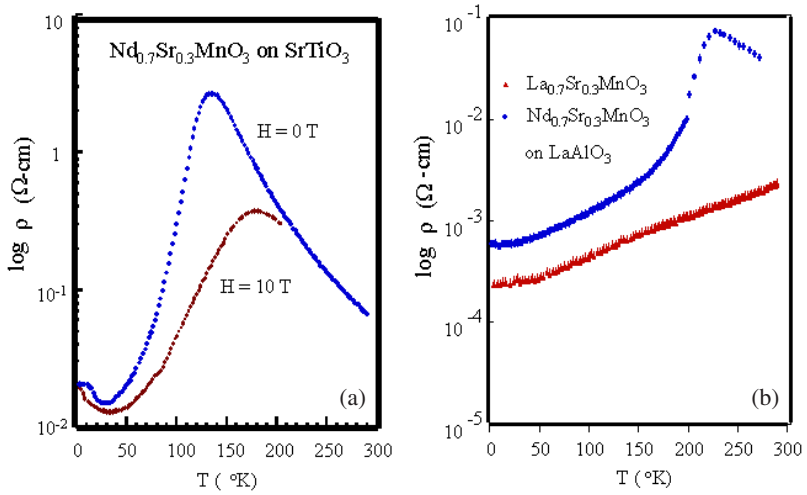

Figure 8. The resistivity versus temperature plots of perovskite manganite samples grown by combinatorial synthesis: (a) $Nd_{0.7}Sr_{0.3}MnO_3$ with $H = 10$ and 0 T; (b) $Nd_{0.7}Sr_{0.3}MnO_3$ and $La_{0.7}Sr_{0.3}MnO_3$ with $H = 0$.

3.1.1. Synthesis. To control film stoichiometry, we deposited a gradient of thickness of precursor layers using *in situ* high-precision shutters, followed by *ex situ* post-annealing. This technique can easily generate precisely controlled stoichiometric profiles within a very small area. This advantage is crucial when various single-crystal substrates need to be used (as in this study) for high-quality epitaxial film growth.

36 CPDs of perovskite manganites ($RE_{1-x}A_xMnO_3$) in epitaxial thin-film form were made, where RE = Y, La, Ce, Pr, Nd, Sm, Eu, Gd, Tb, Er, Tm, Yb, and A = Ca, Sr, Ba, and x is varied continuously from 0 to 1. We made three sets of 36 different phase spreads on six 15 mm by 15 mm substrates of three different single crystals, (100) $LaAlO_3$, (100) $SrTiO_3$, and (110) $NdGaO_3$. As illustrated in figure 7(a), a gradient of RE oxide is deposited at the bottom. After finishing six strips of RE oxide gradients on a substrate, gradients of Mn_3O_4 and $AMnO_3$ were deposited as a middle and top layer. All the precursor films in this study were deposited at room temperature by a high-vacuum ($\sim 10^{-7}$ Torr) pulsed laser deposition (PLD) system. The forward-expanding plume in high vacuum coupled with scanning of a laser beam across the $2'' \times 2''$ targets during deposition resulted in a deposited thickness uniformity of better than 1.5% over a 15 mm × 15 mm area, and therefore ensures accuracy in stoichiometry (easily controlled by a shutter). Following deposition, the sample was annealed at 200 °C for several days before it was annealed at 400 °C for 30 h and then sintered for 2 h at 1000 °C. Low-temperature annealing is necessary to allow homogeneous mixing of precursors into an amorphous intermediate before the crystallization at higher temperatures. Once the synthesis conditions are found, fabrication of these libraries takes only a small amount of time.

In order to study the crystalline quality of the samples, we made individual samples of various compositions selected from the phase diagrams under the same fabrication and processing conditions. In figure 7(b), the $\theta/2\theta$ XRD pattern for $Nd_{0.7}Sr_{0.3}MnO_3$ on an LAO substrate indicates that the film is highly oriented along the c-axis. Even on a logarithmic scale, we can hardly see any other impurity phase. ϕ-scans of the (101) planes indicate that the film is in-plane aligned with the substrate. The narrow width of the peaks indicates the high-quality crystalline formation of the films. We confirmed similar epitaxial growth in many

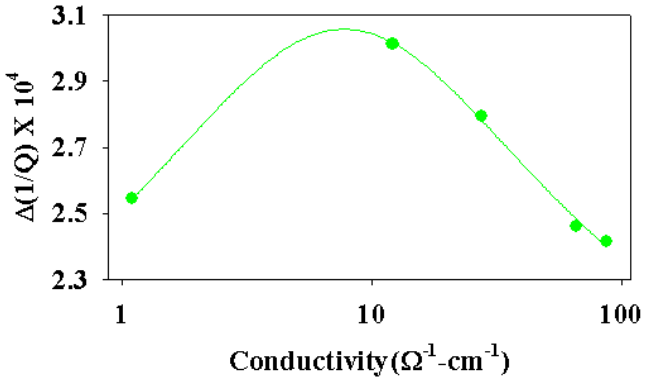

Figure 9. Microwave loss, $\Delta(1/Q)$, versus dc conductivity (Ω^{-1} cm^{-1}). Solid circles were obtained from the measured microwave and corresponding dc responses. The line is the theoretical fit. (Reproduced from [16].)

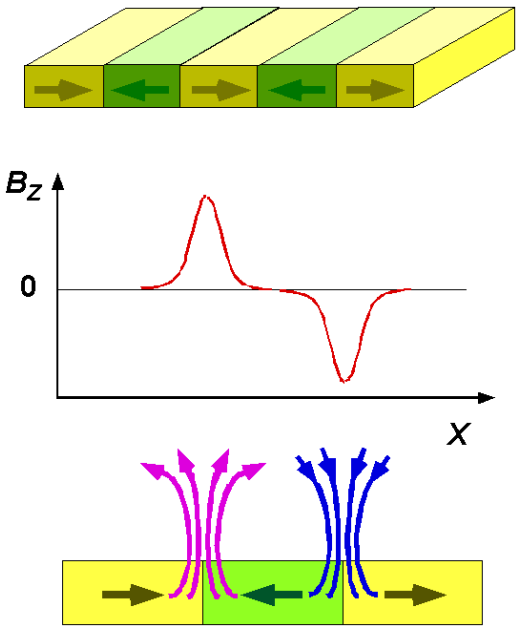

Figure 10. Magnetic domains measured by the SSQM in a thin film with perpendicular magnetization.

different compounds with different hole doping levels.

Figure 8(a) is the resistivity versus temperature plot for selected manganite samples. The transition temperature and resistivity scales are comparable to those from conventional thin-film fabrications. Figure 8(b) shows resistivity versus temperature plots of different samples at zero magnetic fields. The low residual resistivity ratios are the lowest among existing film measurements, and suggest that the films are of high quality.

3.1.2. Characterization. To map the electronic properties of the CPDs, we choose two probes with very different energy scales (by 10^6): visible light and microwaves. The colours roughly

indicate the electronic bandwidths of the compounds. In order to map the electrical impedance at microwave frequencies, we used a scanning EMP operating at 2.2 GHz [19–21]. Briefly, the instrument measures the complex impedance of the probe by monitoring the changes in resonant frequency (f_r) and quality factor (Q) of the cavity. The proximity of a sample to the tip changes the complex impedance of the probe, changing f_r and Q. The shift in f_r is governed, for bulk samples (qualitatively correct for thin-film case involved here), by

$$\frac{\Delta f_r}{f_r} = \sum_{n=1}^{\infty} \frac{bt_n}{a_1 + a_n}$$

where

$$a_n = 1 + \frac{g}{R_0} - \frac{1}{1 + \frac{g}{R_0} + a_{n-1}} \qquad t_n = \frac{bt_{n-1}}{1 + \frac{g}{R_0} + a_{n-1}} \qquad b = \frac{\varepsilon_r + \mathrm{i}\varepsilon_i - \varepsilon_0}{\varepsilon_r + \mathrm{i}\varepsilon_i + \varepsilon_0}$$

where g is the tip–sample gap, R_0 is the tip radius, ε_0 is the permittivity of free space, and ε_r and ε_i are the real and imaginary parts, respectively, of the complex dielectric constant of the sample at f_r. For highly insulating samples ($\varepsilon_i < \varepsilon_r$), $\Delta(1/Q)$ increases while f_r decreases with increasing ε_i. For highly conductive samples ($\varepsilon_i > \varepsilon_r$), both $\Delta(1/Q)$ and f_r decrease with increasing $\varepsilon_i = 4\pi\sigma/\omega$.

To calibrate the microwave signal, we compared the dc resistivity of a number of films to the microwave results. The proximity of a sample to the tip changes the complex impedance of the probe, changing f_r and Q. In this study, the model analysis is based on a first-order approximation, which is valid when the conductivity is low. The shift in resonant frequency is a monotonic increasing function of the conductivity. The shift in quality factor is double valued, approaching zero as the sample becomes insulating or highly conducting. The shift in quality factor has been calibrated against the measured dc conductivity and is consistent with the theoretical analysis. To prevent shorting from the probe tip to the conducting sample, a uniform thin layer of polymer coating was applied on the sample surface. Figure 9 provides a function for converting from a microwave signal to dc conductivity.

To map the magnetic phases at low temperature, we employed a scanning superconducting quantum interference device microscope (SSQM) [22]. A miniature SQUID ring with a diameter of 10 μm was used to scan over the sample surface. In this geometry, the SSQM senses a local magnetic field perpendicular to the surface, B_Z. Since the magnetic moment of a ferromagnetic phase is in plane, the SSQM is limited to the measurement of a field leaked from magnetic domains in the material (figure 10). An oscillating signal indicates the presence of magnetic domains. The periodicity (or width d) is correlated with the domain size, while the amplitude (ΔB_z) is related to the presence of ferromagnetic ordering. The SSQM measurements were performed without an external magnetic field.

3.1.3. Results. Figure 11 is the room temperature charge-coupled device (CCD) photoreflection image of 36 CPDs on three different substrates. Figure 12 shows the detailed measurements of the room temperature microwave impedance of a CPD of $Er_{1-x}Ca_xMnO_3$. First, we observed many clear boundaries in both optical and microwave impedance images. The relevant energy scale of such a transition probed by visible photons is high compared to kT, the thermal energy at room temperature, indicating that the symmetry-breaking order parameter probed here is likely to be electronic in origin. The microwave loss peaks at these boundaries. X-ray data show no evidence of structural phases other than perovskite throughout these CPDs. The existence of these boundaries suggests that complex electronic orderings (with fundamentally different physical properties) occur as a function of x.

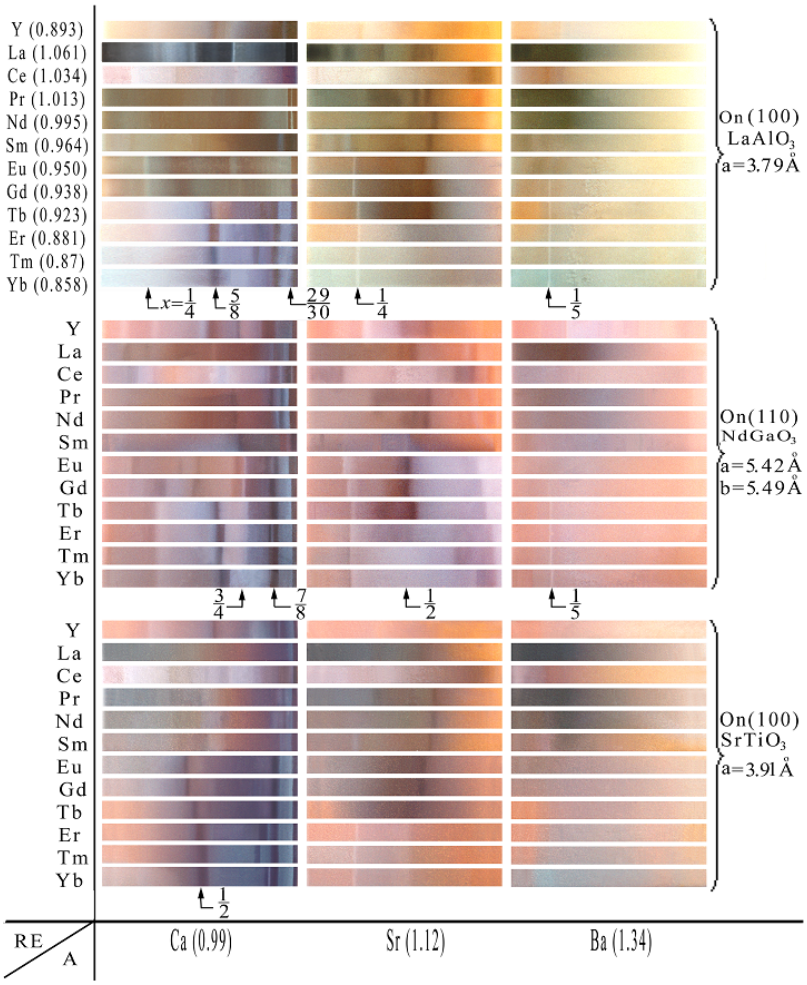

Figure 11. A room temperature CCD colour photograph (photo-reflection image) of 36 $RE_{1-x}A_xMnO_3$ CPDs on $LaAlO_3$, $NdGaO_3$, and $SrTiO_3$ substrates under white light (4.2–7.8 $\times$ 10^{14} Hz). The optical images were taken using a monochrome CCD camera. The parentheses indicate the crystal ionic radii of the elements [53]. The commensurate doping points of singular phases are indicated. The effective unit cell of (110) $NdGaO_3$ has $a' = b' = 3.86$ Å $\left(a' = b' = \frac{\sqrt{(a^2+b^2)}}{2}\right)$.

Second, a very narrow insulating (or more accurately semiconducting) strip within a highly conducting region (appearing as a greyish-blue strip within a black band in figure 11)—around 7/8 doping points of the CPDs of $Tm_{1-x}Ca_xMnO_3$ on $NdGaO_3$ substrate and $Yb_{1-x}Ca_xMnO_3$ on $SrTiO_3$ substrate—was observed at the commensurate charge-filling point $x = 7/8$. The strip is so narrow in phase width that it would have been very difficult to find it using the conventional practice of studying samples of discrete composition.

In figure 13, the CPDs of $Tm_{1-x}Ca_xMnO_3$ for different doping ranges are selected for temperature-dependent comparisons of blue-light (6.2–7.8 $\times$ 10^{14} Hz) reflection images. In strips A and C, as the temperature is raised, the boundary (shown as a peak in intensity) broadens or disappears, indicating the effect of thermal fluctuation. In strip B, as the temperature is

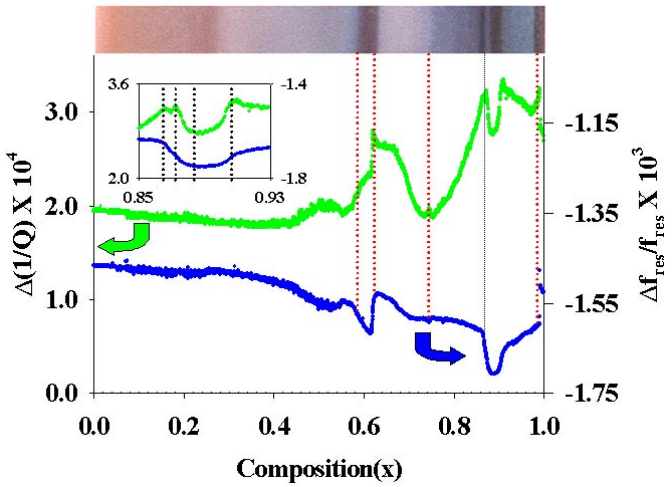

Figure 12. The microwave response of the CPD of $Er_{1-x}Ca_xMnO_3$ on $NdGaO_3$. Microwave loss, $\Delta(1/Q)$, and frequency shift ($\Delta f_{res}/f_{res}$) were measured versus composition (x). The dashed lines are used to indicate phase boundaries. The inset is a 'zoomed' portion near the commensurate singularity (reproduced from [16]).

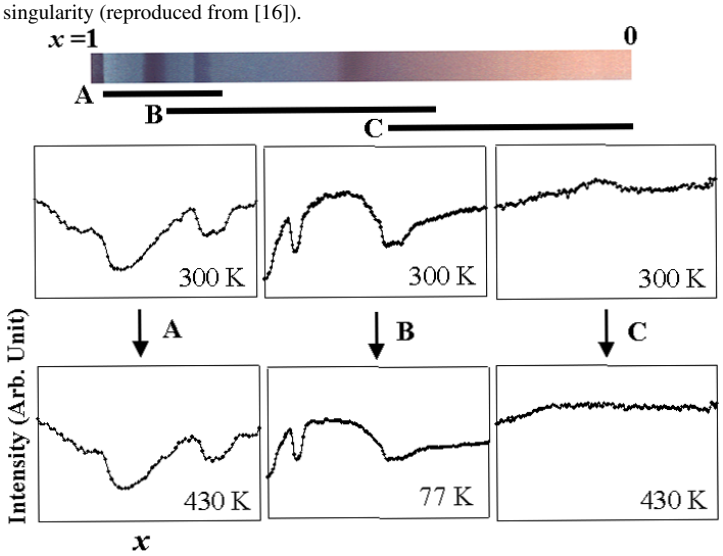

Figure 13. A room temperature CCD colour photograph of $Tm_{1-x}Ca_xMnO_3$ CPD on $SrTiO_3$ under white light. Three doping regions are selected for blue-light ($6.2–7.8 \times 10^{14}$ Hz) photo-reflection at three different temperatures. The optical images were taken using a monochrome CCD camera and a blue filter. White light incident at 60° was used to illuminate the sample and the intensity of the light scattered at 30° was measured as a function of temperature from 77–430 K (reproduced from [16]).

lowered, suppression of intensity in the middle portion is clear. This tends to sharpen the phase boundary towards the right (less doping) of the dark conducting phase. The dip in the conducting phase around $x = 1/2$, also corresponding to a dip in the microwave conductivity measured by the EMP, tends to disappear at low temperatures. In other manganite systems, such as $Nd_{1-x}Sr_xMnO_3$, a similar phase near the $1/2$ doping point was found to have two or more intrinsic competing phases (phase separation) with the charge-ordering phase dominating

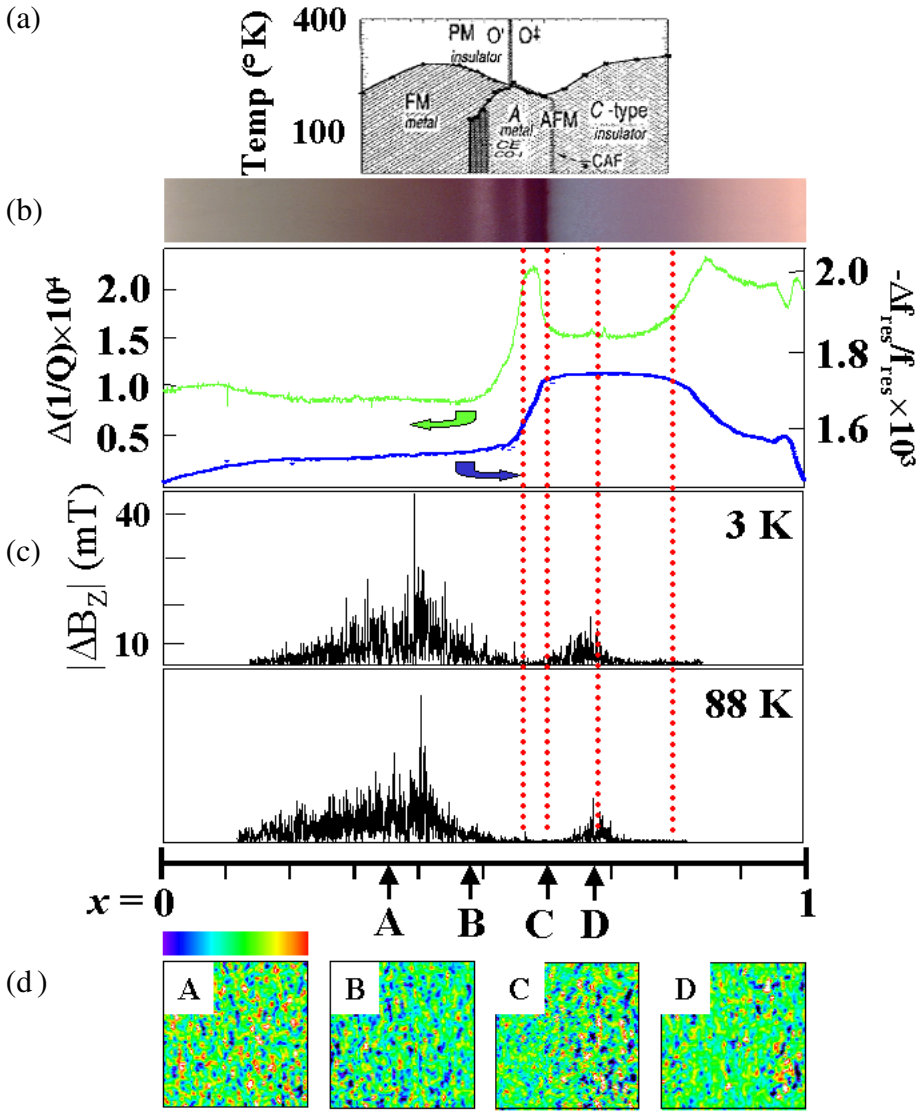

Figure 14. (a) A room temperature CCD colour photograph (photo-reflection image) of the CPD of $Nd_{1-x}Sr_xMnO_3$ on $LaAlO_3$ substrate under white light ($4.2–7.8 \times 10^{14}$ Hz) and the magnetic phase diagram from a single-crystal study [24]. The various states are: paramagnetic insulator (PI), ferromagnetic insulator (FI), ferromagnetic metal (FM), charge-ordered insulator (COI), AFI. (b) The line scan profiles of microwave loss and frequency shift for $Nd_{1-x}Sr_xMnO_3$ film as a function of Sr concentration x measured with a scanning evanescent microwave microscope at room temperature. $\Delta(1/Q)$ increases with increasing microwave loss and $-\Delta f_r/f_r$ increases with increasing tip–sample capacitance. (c) Line scan profiles of perpendicular magnetic field above $Nd_{1-x}Sr_xMnO_3$ film as a function of Sr concentration x measured with a scanning SQUID microscope at 3 and 88 K without an external magnetic field. (d) Magnetic domain structures of $Nd_{1-x}Sr_xMnO_3$ film at 3 K. A colour bar indicates the measured perpendicular magnetic field, B_Z. The scanned areas are 300×300 μm^2 in all images. The Sr content x increases linearly with the horizontal distance in each image. Domain structures of ferromagnetic films are probed with in-plane magnetization. In the present thin-film sample, magnetic moments lie in plane. Thus, the SSQM looks at the magnetic field flowing in or out through domain boundaries. Red and purple regions in the SSQM images correspond to the domain boundaries.

as the temperature is lowered. This indicates that a more homogeneous charge-ordering phase dominates at 77 K, since an insulating and more homogeneous phase should decrease the amount of reflected light. The gradual change in ionic radii induces unexpected abrupt changes in phase patterns. This effect can be observed upon substitutions of different rare-earth and divalent alkaline-earth elements. We see relatively smooth phase patterns and the absence of sharp transition boundaries in the Sr-doped system. This trend is even more pronounced in the Ba-doped system. The clear effect of large band overlap due to the smaller ionic size of Ca is observed in the rich and diverse phase patterns in the Ca-doped system. The effect of substrate-induced stress can also be observed.

Figure 14 is the result of a microwave probe scan and a SSQM scan for the CPD sample of $Nd_{1-x}Sr_xMnO_3$. Previous intensive studies have revealed a rich phase diagram of this system exhibiting a variety of magnetic and metal/insulator transitions [23, 24]. We observed that the optical and microwave properties at room temperature (well above the onset of magnetic order) are clearly correlated with the magnetic properties at low temperature. First, we note that the dark conducting phase between $x = 0.5$ and 0.6 of the CPD clearly matches the A-type antiferromagnetic (in-plane ferromagnetic and out-of-plane antiferromagnetic) metallic (A-AFM) phase found from single-crystal studies. A narrow white strip near $x = 0.5$ coincides with a CE-type charge/spin-order phase [25]. Note that in $Nd_{1-x}Sr_xMnO_3$ there should be no long-range-order phase transitions (symmetry breaking in order parameters of low-energy excitations) at room temperature. The fact that the room temperature electronic boundaries match the low-temperature magnetic boundaries indicates that the electronic ground state (which changes abruptly with composition) dictates the magnetic order at low temperature. Under white light, the A-AFM phase appears dark, suggesting that it is metallic. f_r decreases sharply upon entering this phase, indicating that the conductivity increases. The sample becomes conductive for $x > 0.5$ (an A-AFM phase at low temperature) and remains conductive until $x = 0.8$. The dark phase has a width of 0.052 in x. Afterwards, for $x > 0.8$, the sample gradually becomes insulating. At $x = 0.66$, there are two small peaks which coincide with the boundary between A-type AFM and C-type AF from single-crystal studies [26]. The microwave evidence suggests the onset of high-energy electronic order at room temperature.

In the FI and FM regions with $0 \leqslant x \leqslant 0.5$, ΔB_Z is relatively large, as expected. For ferromagnetic materials, we expect to see large domains with small magnetic fields and narrow domain boundaries where the flux leaks out and can be detected by the SSQM. However, since the resolution of the SSQM is limited to 10 μm, if domain boundaries are less than 10 μm they will appear as wider. The observed domains have almost identical widths, implying that a homogeneous ferromagnetic state is established in this region. ΔB_Z rapidly decreases as x (the content of Sr) approaches 0.5 from the FM side. An abrupt change is visible in the optical image as well. This abrupt change corresponds closely to the $1/2$ charge ordering in single-crystal studies [25]. For $0.5 < x < 0.6$, ΔB_Z is mostly suppressed as expected for an A-type AFM phase, but slightly recovers toward $x = 0.6$, the C-type AF region. In the C-type AF phase, the magnetic moments perpendicular to the plane were thought to be slightly tilted [24]. We expect such canting of the magnetic moments in the antiferromagnetic order to induce a non-zero in-plane magnetization M. This situation is essentially the same as that of FM with in-plane moments, although its M-value is much smaller. It is quite natural that there are in-plane domains visible in the CAF region. Figure 14(c) shows the temperature dependence of the SSQM scan of the CPD. The magnetic profile across the film is essentially temperature independent below 100 K. This result is consistent with the magnetic phase diagram obtained for bulk samples.

As can be seen in figure 14(d), the ΔB_Z values are widely scattered. That is, we observe very intense B-signals from some narrow regions, which are shown in yellow and red in the

figures. The domains in the present CPD of $Nd_{1-x}Sr_xMnO_3$ are very fine, of the order of 10 μm, which is close to the spatial resolution of the SSQM. Furthermore, their size is almost independent of x.

Although there are similarities between previous phase diagram studies (mainly focused on low-temperature long-range-order phases) and inferred CPD data, the very existence of electronic phase transitions has not been observed and studied before, and their nature has not been studied before either. While some of the boundaries exist as smooth crossovers to other phases, some of the boundaries are quite abrupt in both electronic and optical properties. The discovery and study of these boundaries with conventional methods and approaches would be very difficult, if not impossible, due to the intrinsic nature of conventional sample synthesis.

3.1.4. Discussion

Orbital ordering in doped Mott insulators. Upon variation of the carrier density, manganese oxides pass through a variety of magnetically ordered phases at low temperature. These states include:

F: F-type ferromagnetism, in which neighbouring manganese-ion spins are aligned;
A: A-type antiferromagnetism, in which neighbouring manganese-ion spins are ferromagnetic in the plane and antiferromagnetic out of the plane;
C: C-type antiferromagnetism, in which neighbouring manganese-ion spins are antiferromagnetic in the plane and ferromagnetic out of the plane;
G: G-type antiferromagnetism, in which neighbouring manganese-ion spins are antiferromagnetic in three dimensions.

The complexity of the various magnetic and electronic phases can be understood as naturally arising from different orbital-ordered states in this system [27]. Orbital ordering results from the strong spin–orbital coupling in this system. Simply, the coupling of neighbouring orbitals depends on a combination of direct Coulomb and exchange interactions. The orbital coupling determines the overlap of neighbouring orbitals and thereby determines the exchange interactions between neighbouring spins. The d orbitals of the manganese ions are split into e_g and t_{2g} orbitals (figure 15). The two e_g orbitals, in the absence of a Jahn–Teller distortion, are degenerate. The system can be represented by a simplified Hamiltonian of the form

$$H = \sum_{ij} \left[J_{ij}(T_i, T_j) S_i S_j + K_{ij}(T_i, T_j) \right]$$

where T is a pseudo-spin operator denoting the occupancy of the e_g orbitals ($T = 1/2$ for $d_{x^2-y^2}$ and $T = -1/2$ for $d_{3z^2-r^2}$), J_{ij} is the exchange interaction between neighbouring manganese ions, and K_{ij} is the interaction between neighbouring orbitals. The system has been extensively modelled and a variety of orbital-ordered phases are shown to arise.

Maezono [26] *et al* modelled the orbital order of $La_{1-x}Ca_xMnO_3$ as a function of x using a generalized Hubbard model. In addition to the orbital term, they also include a Jahn–Teller distortion, which is needed to stabilize some of the observed states. They find, depending on the bandwidth and doping of the system, a wide variety of orbital-ordered states. Depending on the doping and bandwidth of these systems, several different orbital ordering states can arise, such as:

- $d_{x^2-y^2}$ and $d_{3z^2-r^2}$: generally associated with F-type ferromagnetism;
- $d_{x^2-y^2}$: generally associated with A-type antiferromagnetism;

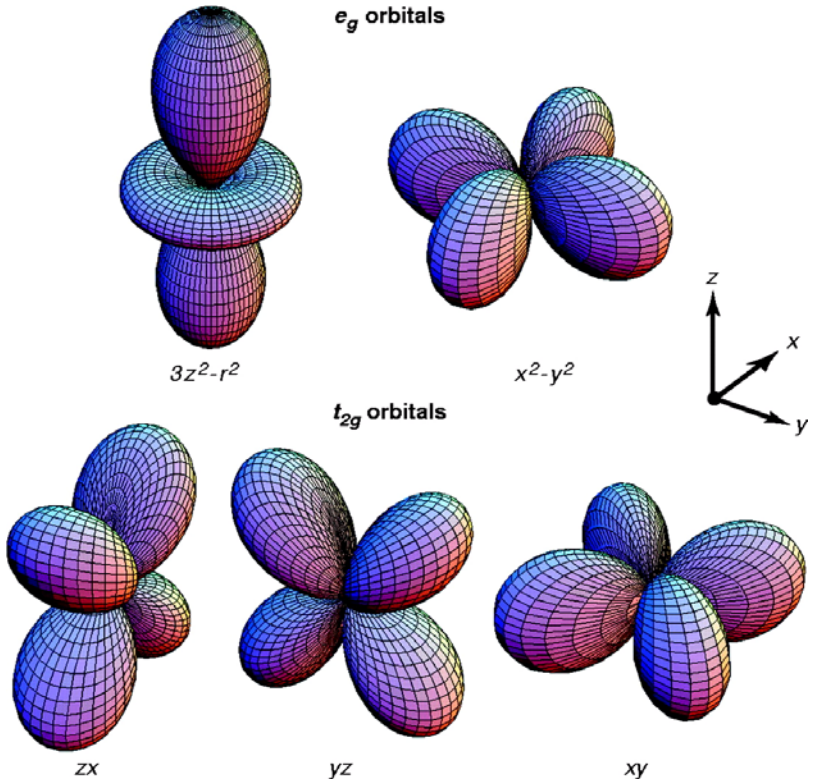

Figure 15. e_g orbitals ($3z^2 - r^2$, $x^2 - y^2$) and t_{2g} orbitals (zx, yz, xy) in manganese oxides. (Reproduced from [27].)

- $d_{3z^2-r^2}$: generally associated with C-type antiferromagnetism;
- $d_{x^2-y^2}$ alternating with $d_{3z^2-r^2}$: associated either with F-type ferromagnetism or G-type antiferromagnetism.

Figure 16 shows the scheme of orbital orderings coupled with possible spin orders. Through its exchange interaction, a given orbital ordering limits possible spin orders. Coupled with spin ordering, orbital ordering will influence conductivity of the system. Generally, as we go from F-type to A- or C-type, conductivity will decrease as the electron conduction is available only in one plane. In G-type, conductivity will further decrease since it is antiferromagnetic in all directions and electron conduction is not favoured, likewise.

Typically, the orbital-ordered state is stable at temperatures greater than those for magnetic order. The modification of the exchange interaction induced in these orbital-ordered phases then determines the spin ordering of the material. The current observation of phase boundaries suggests the existence of different ground states of electronic self-organization due to corresponding orbital states mediated by long-range Coulomb interaction. With the transfer interaction heavily depending on the doping level, various orbital-ordered and disordered states may exist with concomitant spin (and occasionally charge) orders.

For $La_{1-x}Ca_xMnO_3$, extensive modelling has been performed using a mean-field approximation by Maezono *et al* [26]. They find four types of spin order:

- G-type: $x \sim 0$, $x > 0.9$ (three-dimensional antiferromagnetic ordering);

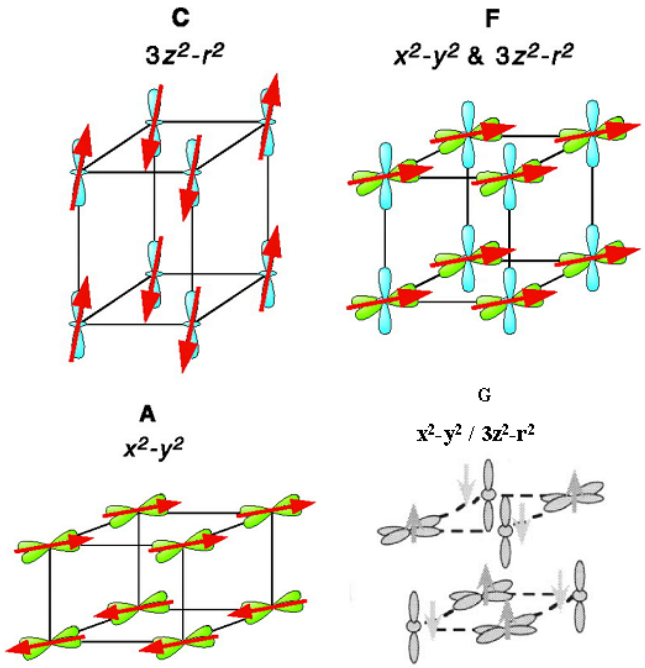

Figure 16. Orbital and corresponding spin orders in perovskite manganese oxides (reproduced from [27]).

- A-type: $0 < x < 0.1$, $0.25 < x < 0.45$ (ferromagnetic in the x–y plane, antiferromagnetic in the z-direction);
- F-type: $0.1 < x < 0.25$ (ferromagnetic);
- C-type: $0.45 < x < 0.9$ (ferromagnetic in the z-direction, antiferromagnetic in the x–y plane).

Figure 17 shows the CPD of $La_{1-x}Ca_xMnO_3$ aligned with the theoretical phase diagram, which displays the orbital orderings in these systems as a function of composition using parameters appropriate for $La_{1-x}Ca_xMnO_3$. It shows the calculated orbital and spin order at various compositions. The correlation between room temperature resistivity and low-temperature magnetic behaviour is consistent with the observation of remnant orbital states. While the existence of residual orbital ordering in these materials is not unexpected, the abruptness of some transitions versus charge filling is remarkable.

With doping x slightly increasing from 0, the abrupt increase in conductivity indicates the predicted transition from G-type order to A-type order. Such increase in conductivity compared to the G-type region ($x \sim 0$) is expected, since A-type ordering is ferromagnetic in the plane. A broad dip in $\Delta(1/Q)$ centred at $x \sim 0.15$ indicates increase in conductivity according to our calibration curve. This dip is presumably the beginning of the transition from A-type to F-type orbital ordering. Since F-type ordering can conduct electrons both in the plane and out of the plane, it attains higher conductivity than A-type ordering. A second broad peak in $\Delta(1/Q)$ centred at $x \sim 0.35$ corresponds to a decrease in conductivity indicating a return to A-type ordering. The broad plateau in $\Delta(1/Q)$ centred at $x \sim 0.75$ may be associated with a transition to a new orbital ordering, presumably C-type. At $x = 0.93$ the abrupt changes in $\Delta(1/Q)$ and f_r indicate an abrupt transition to an insulator. This change strongly suggests a

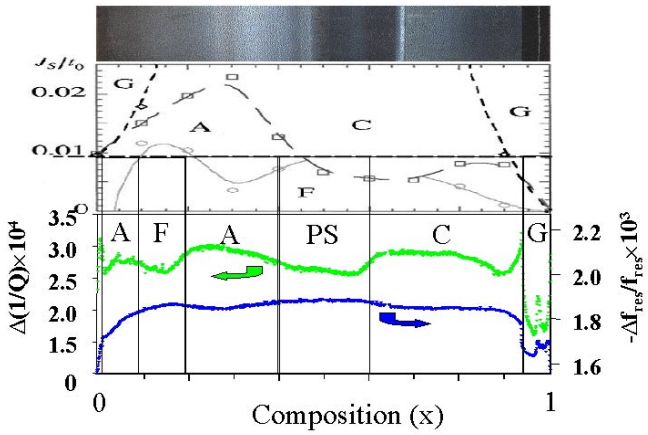

Figure 17. The CPD of $La_{1-x}Ca_xMnO_3$ and calculated orbital spin orders versus charge filling, with the ratio of the bandwidth to the exchange interaction indicated (reproduced from Maezono *et al* [26]). The parameters were chosen to reproduce the results for $La_{1-x}Ca_xMnO_3$.

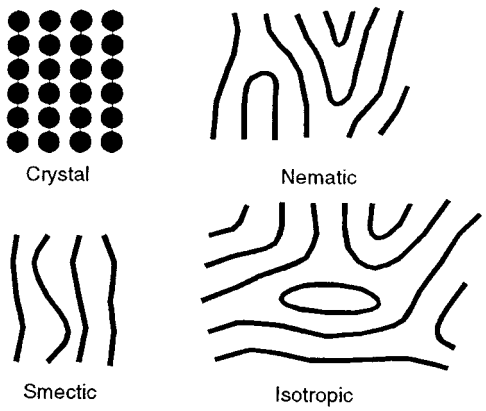

Figure 18. Various phases of stripe order depending on the degree of fluctuation. Heavy lines represent liquid-like stripes, along which the electrons can flow, whereas the filled circles represent pinned, density-wave order along the stripes. (Reproduced from [34].)

transition to G-type antiferromagnetic ordering.

For $x = 0.97$, a narrow highly conducting region appears, while adjacent regions are highly insulating. Such a drastic change in conductivity over a small range in doping cannot be explained by orbital orderings and it has not been observed before in doped Mott insulators. This phenomenon may be common to many highly correlated systems. For studying this type of phenomenon, CPDs are apparently a powerful tool, since they allow the precise exploration of minute changes in composition.

Anisotropic charge orders and stripes in doped Mott insulators. The doped Mott insulators are strongly correlated electronic systems, and the doped carriers tend to self-organize into highly anisotropic patterns (stripe phases for example). It is believed that the dynamical nature of this self-organization in doped Mott insulators plays a crucial role in the origins of some heavily researched phenomena, namely colossal magnetoresistance in manganites and high-T_c superconductivity in cuprates. Recently, two competing phenomena, phase separation and

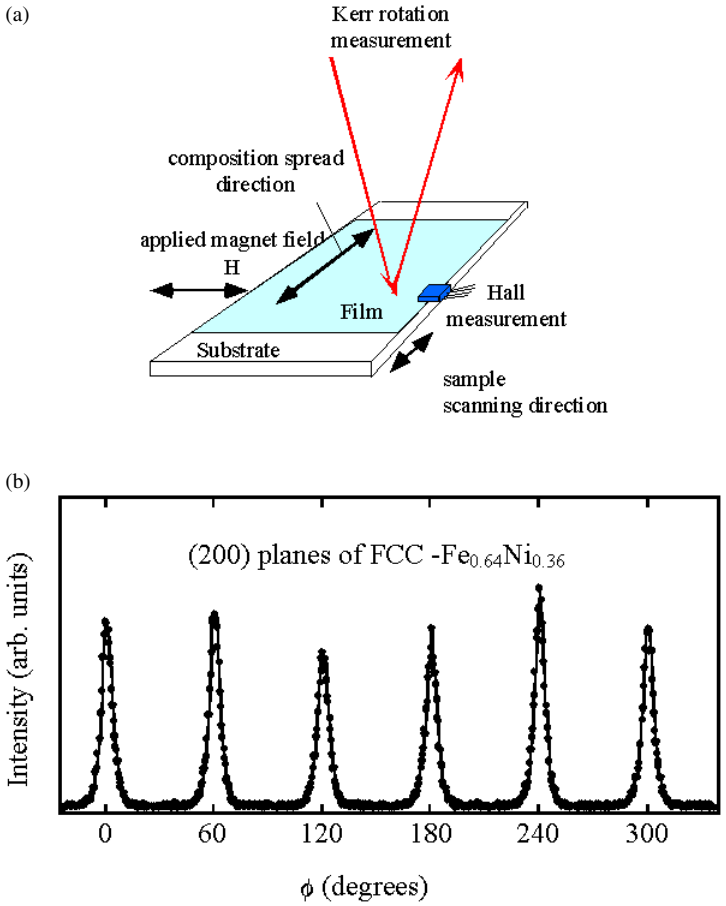

Figure 19. (a) A schematic diagram of the Kerr rotation and Hall probe measurement. (b) An azimuthal (ϕ) scan of the (200) diffraction peak from FCC $Fe_{0.66}Ni_{0.34}$ in the binary CPD.

charge striping, have been observed in these highly correlated systems [28–31]. Upon doping into the parent Mott insulator compounds, the charge carriers tend to separate (at a large scale) into phases of different electronic natures—that is, phase separation occurs [32]. The long-range Coulomb interaction tends to frustrate this phase separation and favour an anisotropic long-range order of charge or spin (a stripe phase, for example) [33]. Note that different charge- or spin-ordered phases are the ground states; these can only be obtained by solving many-body problems for electrons instead of the conventional quasi-particles.

Neutron and x-ray scattering experiments can provide evidence of stripe formation [30,31]. In cuprates, the stripes are believed to be 1/4 filled and inserted between antiferromagnetic 'banks' with transverse periodicity corresponding to the doping level. In manganese oxides, the situation is rather complicated owing to strong coupling of magnetic and electronic states. Here, $Mn^{4+}O_6$ charge stripes are inserted between Jahn–Teller-distorted $Mn^{3+}O_6$ 'parent banks' (also antiferromagnetically paired as in cuprates) with periodicity corresponding to the carrier doping.

Kivelson [34] and collaborators proposed the stripe structures called 'electronic liquid crystals'. Charge stripes (insulating charge-density waves) tend to prevent superconductivity

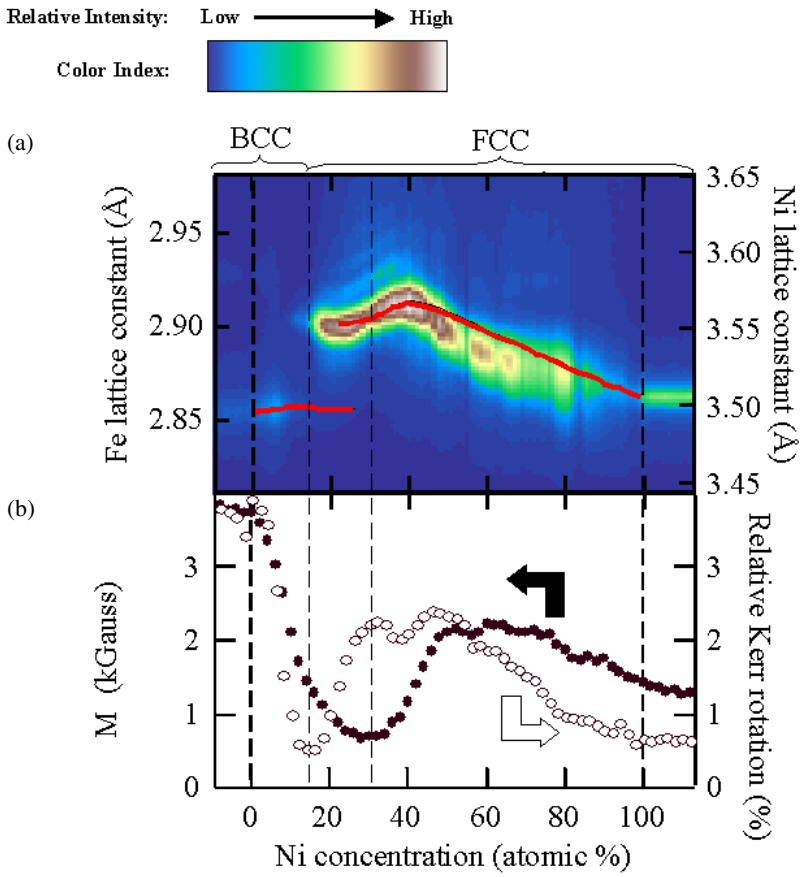

Figure 20. (a) An x-ray intensity map of the surface-normal d-spacing obtained by radial (θ–2θ) scans along the surface-normal direction. The observed d-spacings are converted to lattice constants. The superimposed curve shown in red indicates the bulk discrete-composition results calculated from previously reported lattice constants at 15 °C for both BCC (α-phase) and FCC (γ-phase) Fe–Ni alloys [42, 44]. (b) The saturation magnetization (M_s) obtained with a scanning Hall probe, and the relative Kerr rotation obtained from SMOKE measurements for the longitudinal configuration at a wavelength of 6328 Å (He–Ne laser) (reproduced from [18]).

rather than promote it. Kivelson *et al* circumvent this problem by allowing fluctuating stripes, which tends to break the phase locking between adjacent stripes and induce conduction. They predict a variety of stripe phases with differing degrees of symmetry. Depending on the importance of fluctuations, various stripe phases form (figure 18). In the absence of fluctuation, we end up with a Wigner crystal where 2D modulated electrons are locked in phase. If the fluctuation is large enough, the stripes stop being phase locked to each other. This smectic phase or electronic liquid-crystal phase induces a translational symmetry in one direction. In this case, electrons can travel along the stripe, but not in the transverse direction. A recent experiment on cuprates seems to suggest that this kind of anisotropic transport does exist in the system. As fluctuations increase further, the stripes bend, and the resulting nematic phase has translation and reflection symmetries. Finally, the liquid phase breaks no spatial symmetry and, in the absence of disorder, is believed to be a conductor or a superconductor.

In manganese oxides the active orbital degree of freedom induces the highly anisotropic

electron-transfer interaction, which gives rise to complex spin–orbital coupling effects (including stripe phases) [26, 27]. Similarly, the electronic boundaries that we observe in the CPD sample of $Er_{1-x}Ca_xMnO_3$ can be matched to the boundaries of orbital orderings predicted by Maezono *et al* with suitable antiferromagnetic interaction levels. However, the singular phases around $x = 7/8$ in the CPD of $Er_{1-x}Ca_xMnO_3$ on $NdGaO_3$ substrate and $Yb_{1-x}Ca_xMnO_3$ on $SrTiO_3$ substrate are intriguing (figure 12). The existence of such singularity is not predicted by phase diagram calculations of orbital orderings. A possible scenario for the current observation of phase boundaries is electronic self-organizations of different types. Note that around $x = 1/2$ and $7/8$, we would expect commensurate locking of orbital (charge) orderings to the lattice, which would be an insulator. This commensurate singularity point is related to the static charge (or spin) orderings observed in recent experimental and theoretical studies of both copper oxides [30, 31, 33–36] and manganites [27, 29, 37, 38]. We expect to see a small structural anomaly associated with the singularity, owing to the strong coupling of charge ordering to the lattice at the commensurate point. If we accept this model, the highly conducting adjacent regions then suggest the existence of incommensurate, fluctuating orbital orderings. Therefore, the current observation provides preliminary evidence of the recently proposed liquid-crystal phase (smectic phase) of orbital orderings in this doping range, widely believed to exist in copper oxides [34]. The smeared-out critical divergence in microwave loss at the boundaries observed in this study is also consistent with this possibility. The thermodynamic nature of the transition is clearly shown by the temperature-dependent broadening or disappearance of the phase boundaries at higher temperatures. However, we believe that more studies are needed to confirm this suggestion.

3.2. CPDs of structure–property relations of $Fe_{1-x}Ni_x$ metallic alloys

The central theme and focus of the combinatorial materials science approach have been combining parallel synthesis with rapid characterization techniques to map out physical or chemical properties as functions of composition for a given system. The question remains of whether it is feasible to map the complex relationship between lattice structure and physical properties as a function of composition for a multi-component system in one experiment. Addressing this issue, we carried out a detailed mapping of the crystal structure and physical properties of the well-documented $Fe_{1-x}Ni_x$ binary alloy system on a single material chip with linear composition x changing from zero to one [18]. This system is of interest because it shows a BCC-to-FCC transformation with increasing x as well as rich changes in the magnetic properties with x.

3.2.1. Synthesis and characterization. The method used to deposit the Fe/Ni multi-layered films, using an ion-beam-sputtering, combinatorial deposition system, was similar to that employed to establish the CPD of manganites on sapphire (0001) substrates ($\sim$1 cm long) at room temperature. The system has a deposition chamber with base pressure of 10^{-10} Torr and a load-lock chamber for exchanging the sample substrate without breaking the vacuum. Ar ions with an acceleration voltage of 1000 eV are used as an incident beam, and a typical deposition rate of 0.3 Å s^{-1} for Ni and Fe targets can be achieved. As-grown multi-layered films were annealed at 600 °C for 3 h in evacuated ampoules to obtain full compositional mixing normal to the film plane without oxidation and to achieve alloy phase formation. The samples were air quenched after annealing. Auger depth-profile analysis of the annealed sample shows uniform profiles of Ni and Fe concentration across the thickness of the film, in contrast to the stepped layer profiles for the as-deposited sample. This suggests that the layered films are thoroughly mixed within the thickness of the film. Without a capping layer, a slight oxidation

is expected on the top, but the characterizing probes penetrate far enough into the film to measure essentially bulk properties of the sample.

The crystal structure of the sample was measured at Argonne National Laboratory using x-ray diffraction with small-beam irradiation at the SRI-CAT 2-BM bending-magnet beamline of the advanced photon source. The beam size used was 50 μm along the composition-spread direction. Magnetic properties were measured with a scanning Hall probe and scanning magneto-optical Kerr effect (SMOKE) measurements with spatial resolution of less than 200 μm (figure 19(a)).

3.2.2. Results and discussion. The CPD chip exhibited two dominant crystal structures. The Ni-rich alloys form a FCC structure (γ-phase) and the Fe-rich alloys form a BCC structure (α-phase). The structural phase transition between the α-phase and the γ-phase occurs around $x = 0.12$ (with a rather broad two-phase overlap range from $x = 0.08$ to 0.18). Both structures were found to be 'rotationally' epitaxial to the underlying sapphire (0001) substrate. For the γ-phase, its [111] and [$1\bar{1}0$] axes were found to be aligned with the [0001] and [$\bar{1}100$] axes of the substrate, respectively. Due to the sixfold rotational symmetry of the substrate lattice, all six rotationally equivalent domains were found. A typical transverse (ϕ) scan result is shown in figure 19(b). While the in-plane mosaic spread of the film was relatively poor (about 5° in FWHM), the surface-normal mosaic spread was excellent (narrower than 0.1° in some regions of the film). The α-phase alloy exhibited different but related rotational epitaxy. Its [110] direction was found to be parallel to the [111] axis of the γ-phase. As we will show later, the alignment of the [110] axis of the Fe-rich α-phase with the [111] axis of the Ni-rich γ-phase is a consequence of the near coincidental matching of their lattice constants such that $a_\alpha/\sqrt{2} \approx a_\gamma/\sqrt{3}$. In addition, the [$1\bar{1}0$] axis of the Fe-rich alloy was found to be parallel to the [$11\bar{2}0$] axis of the substrate. Because of the twofold rotational symmetry of the γ-phase structure in the plane normal to the [110] axis, a total of 12 equivalent rotational domains were found on the substrate with sixfold rotational symmetry. The epitaxial growth is important here for number of reasons. First, it made it possible to study off-specular diffraction, which allowed the determination of the crystal structures (in this case, distinguishing the γ-phase and α-phase). Second, well-oriented films of high quality allow reliable characterization of physical properties.

While the Ni-rich and Fe-rich alloys retain their respective epitaxial orientations, the lattice constant of the $Fe_{1-x}Ni_x$ system varies non-linearly throughout the CPD chip. Figure 20(a) shows the specular diffraction pattern of the sample. The contour map and coloured intensity profiles were generated by a series of linear scans with the momentum transfer (q) perpendicular to the substrate (0001) plane. The $\theta_\perp$ scan revealed only the (111) diffraction peak from the Ni-rich γ-phase and the (110) peak from the Fe-rich α-phase due to the excellent texture of the sample. Because of the anisotropic stresses in the thin-film sample, the cubic structures of both phases are slightly distorted, so the lattice parameters obtained from the diffraction peak normal and parallel to the substrate crystal plane are slightly different (by a few per cent). For simplicity, however, we converted the measured d-spacings perpendicular to the substrate crystal plane into BCC and FCC lattice parameters using the relationship $a_{\mathrm{BCC}} = \sqrt{2}d_{110}$ and $a_{\mathrm{FCC}} = \sqrt{3}d_{111}$. The regions on the left of 0% and the right of 100% of atomic Ni concentration correspond to the pure Fe and Ni phases, respectively. The Ni concentration was assumed from the growth conditions and confirmed by Auger analysis. In these regions, the positions of the diffraction peak remain constant and the measured lattice constants are consistent with the reported bulk lattice constants of pure Fe and Ni. The solid lines in figure 20(a) indicate the previously reported lattice constants for the discrete-composition samples [39, 40]. Our data for the CPD chip reproduce all the important features in the lattice constant–composition curve.

For example, the phase transition from BCC to FCC in bulk samples does not occur abruptly, similarly to our observation. Moreover, the local maxima and the inflection point observed in bulk sample studies are also reproduced in our CPD data. Our data, however, do present some minor quantitative discrepancies. For example, the phase transition starts at slightly lower Ni concentration in our CPD sample compared to the previous data obtained from bulk samples. This can be attributed to the stabilizing effect of the γ-phase at lower Ni concentration because the hexagonal symmetry of the substrate is likely to lower the interfacial energy of the FCC structure of the γ-phase. In addition, the lattice constants measured from our CPD chip are consistently smaller in the range $x = 0.1$–0.9. Moreover, our data exhibit some deviation from the linear decrease of the lattice constant over $x = 0.5$–0.9, probably due to the larger degrees of strain density present in this region of the film. The extent of strain in the CPD chip is evident from the broadening of the diffraction peak [41]. It must be noted that strain influence between neighbouring regions is expected. However, the range of such a strain field is largely governed by the grain size, which is well below the resolution of the measurement probes. Figure 20(a) clearly shows the evolution of the peak width as a function of Ni concentration. In particular, the peak width at $x = 0.6$–0.8 is 2–3 times broader than that for the other region of Ni concentration and 4 times larger than that for the pure Ni phase. It is in this region that the lattice constant of the CPD compositions deviates most from that of the bulk study.

The relative saturation magnetization (M_s) and Kerr rotation measured by the scanning Hall probe and using the SMOKE, respectively, are plotted in figure 20(b). The value of M_s is relative because the Hall probe detects the perpendicular ((0001) plane of the substrate) component of the magnetic field near the edge of the magnetically saturated film. A dip in M_s at around $x = 0.3$ was observed; the composition of the dip agrees well with the results of Yensen [42] and Masumoto [43]. This dip is generally associated with the Invar behaviour near (but not at) the FCC–BCC transition [40,44,45]. Such a dip is due to a magnetic phase transition to a mixed phase consisting of both ferromagnetic and antiferromagnetic regions [46]. The shape of the magnetization versus composition curve is known to depend markedly not only on the fabrication and heat treatment of the alloys, but also on the applied field intensity [47]. In our case, the shape of the M_s dip measured with an applied field intensity of 150 Oe is very similar to that reported by Bozorth measured under a similar field intensity [48].

The relative Kerr rotation shows a quite different composition dependence to M_s. A very steep dip was observed at around $x = 0.14$, coincident with the substantially discontinuous phase boundary (figures 20(a) and 20(b)) determined by x-ray study. In general the magneto-optic Kerr effect depends on M_s with slightly different power dependences in different materials. For example, the longitudinal Kerr rotation angle θ_K was found to vary with M_s as $\theta_K \sim (M_s)^{1.7-2.1}$ within FCC phases of different compositions [48, 49]. The steep dip at $x = 0.14$ suggests an anomaly in the Kerr rotation at the structural phase transition. This is not surprising, because the Kerr effect arises from the spin–orbit coupling and can be quite sensitive to the symmetries of the electronic structure and crystal structure [50]. In particular, the Kerr effect arises from interband transitions that couple states of different angular momentum. The dip in the Kerr rotation being coincident with the structural transformation suggests that the same states as are involved in the Kerr effect may also be driving the structural transformation in a Jahn–Teller sense. Our observation of anomalous Kerr rotation at the first-order structural phase transition suggests that this anomaly may be used to study the structural phase transitions in other systems.

4. Conclusions

The rich phase diagrams found for various manganese oxides reflect the complex interactions which determine the electronic ground state. Phase mapping in condensed matter physics is accomplished by growing single-crystal samples and measuring their physical properties at different temperatures. The famous phase diagram of $La_{1-x}Ca_xMnO_3$ took several years to construct. Technologically the location of the phase boundaries is critical in any development and optimization of materials. Obviously if we can produce a proper probe to manifest these phase boundaries and their physical nature, the immediate benefit to the physical understanding of its material system and possibly the very mechanism of the phenomenon of interest is obvious. The impact of the current study is clear in that we can continuously and spatially realize the doping dependence of complex materials.

The observation that transitions between different electronic states at room temperature seem to drive the low-temperature magnetic order is intriguing. In the similar system of high-T_c superconductors, one also finds a rich phase diagram versus doping and temperature. It would be interesting to see whether such phenomena occur in the high-temperature superconductors. Study in this direction may help to resolve the current debate on whether short-range Coulomb interactions lead to an exchange–interaction–pairing mechanism [51, 52] and whether long-range Coulomb interactions lead to dynamic charge stripes and a smectic phase [30, 34]. If doping-dependent electronic boundaries are also present in high-T_c cuprates such as $La_{2-x}Cu_xO_4$, a detailed study of the system at low temperature can be carried out and may reveal suspected quantum critical behaviour at the critical doping points such as $x = 1/8$.

In addition, our first demonstration of mapping the detailed relationship between structural and physical properties using thin-film CPDs has generated convincing evidence that the central issue of materials science can be also addressed with considerably increased efficiency. Our data for the CPD chip demonstrate good overall agreement with the previous data obtained for Fe–Ni alloys of discrete compositions. The minor discrepancies between the present and previous data reveal opportunities for further study, because they point to possible anomalies in the structure and properties of the composition-spread thin films. Knowledge of the overall behaviour and detailed discrepancies due to different substrates or annealing effects of structure–physical property relationships for a given material system are extremely useful to academic research and industrial applications. For example, magnetic alloys, such as Fe–Ni alloys, are used widely in the information industry in a thin-film format. The knowledge derived from bulk sample study alone is often insufficient for device development. Our approach provides a systematic and highly efficient means to shorten the material/device development cycle.

Extension of the current CPD technique to other material systems may be carried out. The effectiveness of the CPD technique seen here suggests that mapping the global properties of a condensed matter system, once thought an intractable problem, is now scientifically achievable.

Acknowledgments

I would like to acknowledge the important contributions from Drs Peter G Schultz, Chen Gao, Ichiro Takeuchi, Ted Sun, Tsuyoshi Ohnishi, Hauyee Chang, and Fred Duewer to this project. This work was supported by the Director of Advanced Energy Projects Division, Office of Computational and Technology Research, US Department of Energy, under contract DE-AC03-76SF00098, DARPA, contract No MIPR98-0765, and the Office of Naval Research, contract No N00014-95-F-0099.

References

[1] Xiang X-D 1999 *Annu. Rev. Mater. Sci.* **29** 149
[2] Xiang X-D 2001 *Handbook of Advanced Electronic and Photonic Materials and Devices* vol 1, ed H S Nalwa (San Diego, CA: Academic) pp 257–77
[3] Scheel H J 1994 *Mater. Res. Soc. Bull.* **19** 26
[4] Phillips J C 1989 *Physics of High-T_c Superconductors* (New York: Academic)
[5] Wu M K, Ashburn J R, Torng C J, Hor P H, Meng R L, Gao L, Huang Z J, Wang Y Q and Chu C W 1987 *Phys. Rev. Lett.* **58** 908
[6] Cava R J *et al* 1990 *Nature* **345** 602
[7] Xiang X-D, Sun X, Briceño G, Lou Y, Wang K-A, Chang H, Wallace-Freedman W G, Chen S-W and Schultz P G 1995 *Science* **268** 1738
[8] Briceno G, Chang H, Sun X, Schultz P G and Xiang X-D 1995 *Science* **270** 273
[9] Jin S *et al* 1994 *Science* **264** 413
[10] Jin S, O'Bryan H M, Tiefel T H, McCormack M and Rhodes W W 1995 *Appl. Phys. Lett.* **66** 382
[11] Hasebe M and Nishizawa T 1978 *Application of Phase Diagrams in Metallurgy and Ceramics (NBS Special Publication)* vol 2 (Washington, DC: US Government Printing Office) pp 911–54
[12] Romig A D Jr 1987 *Bull. Alloy Phase Diagr.* **8** 308
[13] Kennedy K, Stefansky T, Davy G, Zackay C F and Parker E R 1965 *J. Appl. Phys.* **36** 3808
[14] van Dover R B, Schneemeyer L F and Fleming R M 1998 *Nature* **392** 162
[15] Chang H, Takeuchi I and Xiang X-D 1999 *Appl. Phys. Lett.* **74** 1165
[16] Yoo Y K, Duewer F W, Yang H, Yi D and Xiang X-D 2000 *Nature* **406** 704
[17] Yoo Y K, Duewer F, Fukumura T, Yang H, Yi D, Chang H, Hasegawa T, Kawasaki M, Koinuma H and Xiang X-D 2001 *Phys. Rev.* B **63** 224421
[18] Yoo Y K, Ohnishi T, Wang G, Duewer F W, Xiang X-D, Chu Y S, Mancini D C, Li Y Q and O'Handley R C 2001 *Intermetallics* **9/7** at press
[19] Gao C, Wei T, Duewer F W, Lu Y and Xiang X-D 1997 *Appl. Phys. Lett.* **71** 1872
[20] Gao C and Xiang X-D 1998 *Rev. Sci. Instrum.* **69** 3846
[21] Gao C, Duewer F W and Xiang X-D 1999 *Appl. Phys. Lett.* **75** 3005
[22] Morooka T, Nakayama S, Odawara A, Ikeda M, Tanaka S and Chinone K 1999 *IEEE Trans. Appl. Supercond.* **5** 3491
[23] Moritomo Y, Akimoto T, Nakamura A, Ohoyama K and Ohashi M 1998 *Phys. Rev.* B **58** 5544
[24] Kajimoto R, Yoshizawa H, Kawano H, Kuwahara H, Tokura Y, Ohoyama K and Ohashi M 1999 *Phys. Rev.* B **60** 9506
[25] Kuwahara H, Tomioka Y, Asamitsu A, Moritomo Y and Tokura Y 1995 *Science* **270** 961
[26] Maezono R, Ishihara S and Nagaosa N 1998 *Phys. Rev.* B **58** 11 583
[27] Tokura Y and Nagaosa N 2000 *Science* **288** 462
[28] Uehara M, Mori S, Chen C H and Cheong S-W 1999 *Nature* **399** 560
[29] Mori S, Chen C H and Cheong S-W 1998 *Nature* **392** 473
[30] Tranquada J M, Sternlieb B J, Axe J D, Nakamura Y and Uchida S 1995 *Nature* **375** 561
[31] Tranquada J M, Axe J D, Ichikawa N, Moodenbaugh A R, Nakamura Y and Uchida S 1997 *Phys. Rev. Lett.* **78** 338
[32] Moreo A, Yunoki S and Dagotto E 1999 *Science* **283** 2034
[33] Emery V J and Kivelson S A 1993 *Physica* C **209** 597
[34] Kivelson S A, Fradkin E and Emery 1998 *Nature* **393** 550
[35] Noda T, Eisaki H and Uchida S 1999 *Science* **286** 265
[36] Zhou X J, Bogdanov P, Kellar S A, Noda T, Eisaki H, Uchida S, Hussain Z and Shen Z-X 1999 *Science* **286** 268
[37] Chen C H and Cheong S-W 1996 *Phys. Rev. Lett.* **76** 4042
[38] Kuwahara H, Tomioka Y, Moritomo Y, Asamitsu A, Moritomo Y and Tokura Y 1996 *Science* **272** 80
[39] *A Handbook of Lattice Spacing and Structures of Metal Alloys* 1958 ed W B Pearson (New York: Pergamon) ch 11
[40] O'Handley R C 2000 *Modern Magnetic Materials* (New York: Wiley) p 220
[41] Warren B E and Averbach B L 1950 *J. Appl. Phys.* **21** 595
[42] Yensen T D 1920 *J. Am. Inst. Electr. Engrs* **39** 396
[43] Masumoto H 1929 *Sci. Rep. Tohoku Imp. Univ.* **18** 195
[44] Dumpich G, Kästner J, Kirschbaum U, Mühlbauer H, Liang J, Lübeck T and Wassermann E F 1992 *Phys. Rev.* B **46** 9258
[45] Schumann F O, Willis R F, Goodman K G and Tobin J G 1997 *Phys. Rev. Lett.* **79** 5166

[46] Freeland J W, Grigorov I L and Walker J C 1998 *Phys. Rev.* B **57** 80
[47] Bozorth R M 1951 *Ferromagnetism* (New York: Van Nostrand-Reinhold) ch 5
[48] Sato T, Simatsu T, Miyahara T and Miyazaki T 1991 *IEEE Trans. J. Magn. Japan* **6** 869
[49] Miyahara T and Takahashi M 1976 *Japan. J. Appl. Phys.* **15** 291
[50] Liu Z Q and Bader S D 2000 *Rev. Sci. Instrum.* **71** 1243
[51] Scalapino D J 1999 *Science* **284** 1282
[52] Dai P, Mook H A, Hayden S M, Aeppli G, Perring T G, Hunt R D and Dogan F 1999 *Science* **284** 1344
[53] *CRC Handbook of Chemistry and Physics* 1997 79th edn, ed D R Lide (Cleveland, OH: Chemical Rubber Company Press) ch 12